NOVA SCHOOL OF SCIENCE & TECHNOLOGY

DEPARTMENT OF MATERIALS SCIENCE

LOURENÇO MIGUEL PIRES CABRAL

BSc in Micro and Nanotechnology engineering

DEVELOPMENT OF AN INTEGRATED ARRAYED WAVEGUIDE GRATING BUILDING BLOCK ON THE LITHIUM NIOBATE-ON-INSULATOR PLATFORM

MASTER IN MICRO AND NANOTECHNOLOGIES ENGINEERING

NOVA University Lisbon
October, 2022

NOVA SCHOOL OF
SCIENCE & TECHNOLOGY

DEPARTMENT OF
MATERIALS SCIENCE

DEVELOPMENT OF AN INTEGRATED ARRAYED WAVEGUIDE GRATING BUILDING BLOCK ON THE LITHIUM NIOBATE-ON-INSULATOR PLATFORM

LOURENÇO MIGUEL PIRES CABRAL

BSc in Micro and Nanotechnology engineering

Adviser: Prof. Dr. Rachel Grange
Professor, ETH Zürich University

Co-advisers: Prof. Dr. Luís Pereira
Professor, NOVA University Lisbon

Dr. Marc Reig Escalé
Post-Doc, ETH Zürich University

Dr. Alfonso Martínez García
Post-Doc, ETH Zürich University

Examination Committee

Chair: Prof. Dr. Rodrigo Ferrão de Paiva Martins
Professor, NOVA University Lisbon

Rapporteurs: Prof. Dr. Alessandro Fantoni
Professor, ISEL

Prof. Dr. Luís Pereira
Professor, NOVA University Lisbon

MASTER IN MICRO AND NANOTECHNOLOGIES ENGINEERING

NOVA University Lisbon
October, 2022

Development of an Integrated Arrayed Waveguide Grating Building Block on the Lithium Niobate-on-Insulator platform

This document was created with the (pdf/Xe/Lua)LaTeX processor and the NOVAthesis template (v6.10.5) [32].

Parentibus meis.

Acknowledgments

In this section, I express my acknowledgement of the people and acts that supported this project and the journey through time that brought me here. Starting in the experience of developing my master thesis at ETH Zürich and going back to my education and childhood memories that shaped me. Firstly, I want to thank Professor Rachel Grange for the opportunity of developing my thesis at ETHz, in particular in the Optical Nanomaterial Group (ONG). Belonging to the remarkable ETHz University, ONG follows the path of excellence in its inquisitive performance. A group with vast knowledge on photonics and the novel material of Lithium Niobate, whose hospitality was warming and instructive. Prof. Rachel is very intrigued and excited about the development of physics and photonics, such curiosity and interest are very contagious and motivating. Dr. Marc Reig Escalé and Dr. Alfonso Martínez García provided important support to this project, for chip fabrication at FIRST (ETH Zürich) and BRNC (IBL Zürich) cleanrooms, to the guidance and planning that enables proper research to be carried out. Two people with different approaches, whose teamwork is so fruitful. With them, I learned a lot, not only in regard to optoelectronics and PICs but also in how to manage and organize people and work priorities in a professional environment. I could not be more thankful for all I've learned and for all their support throughout the last six months, and for sharing with me their vision of the recently launched company Versics AG, destined to establish LNOI modulators in the telecom industry, I will surely keep hearing this name. At my home university, I am thankful for Professor Luís Pereira that has accepted to be my advisor, quite close to the time of submitting the thesis. At the beginning of this project, I was advised by Prof. Elvira Fotrunato, and I also acknowledge that. At last, I am also incredibly thankful to all the professors that crossed my path at NOVA university in particular at the Material Sciences Department. Since this master thesis is the end of an important chapter of my life course, I feel it is relevant not only to be thankful to the people that helped me throughout these past six months but also to the ones that shaped me into being in this position. I could not begin to recall and acknowledge every great man and woman who has achieved so much in all the studies of the universal axioms. Yet they have been crucial for our time and age and for setting a powerful example that we must all strive to honour.

I will then focus on my personal teachers who made me into who I am. I am thankful for the inspiration set by my godmother, who is a living example that anyone should have various interests and an adventurous spirit. To my close friends with whom I have grown my own adventurous spirit and my capability to dialogue and reason. To the most special of them, I could not be more grateful. with whom my destiny has been intertwined with. For she sees in me the future that I strive to become. My family has been very present and important in my upbringing, as it should be. I am a reflection of that healthy relationship and I am thankful for that. In particular, my grandparents, who taught me how pure can a loving heart be. Last, but definitely not least, my parents deserve my deepest gratitude, for if I can one day be a complete man, it is because of the tools they gave me.

“If I have seen further it is by standing on the shoulders of Giants.” *(Sir Isaac Newton)*

Abstract

The Arrayed Waveguide Grating (AWG) is a passive optical device capable of Multiplexing, Demultiplexing and Routing. It is a very important device for Wavelength Division Multiplexing, in this case interesting for achieving a transceiver of high modulation speeds integrated on-chip. Here an AWG is designed, simulated and characterized in the X-cut Lithium Niobate-On-Insulator (LNOI) platform. Proving for the second time the LNOI is a versatile platform capable of allowing the Integration of AWG. The constraints and required optimizations were analysed to be able to develop an AWG of higher performance in this platform. Here, simulations are presented informing about the physics of the device and the crucial design parameters. It was demonstrated a functional 9x9 AWG in the X-cut LNOI for the C-band, with a channel spacing of 0.9 nm and a 21 dB Insertion Loss.

Keywords: Arrayed Waveguide Grating, Free Propagation Region, Integrated Optics, Lithium Niobate-On-Insulator, Phased Array, Rowland Circle.

Resumo

O Arrayed Waveguide Grating (AWG) é um dispositivo óptico passivo capaz de multiplexação, desmultiplexação e roteamento. É um dispositivo muito importante para Multiplexação por Divisão de Comprimento de Onda, neste caso interessante para conseguir um transceptor de altas velocidades de modulação integrado em chip. Nesta tese, um AWG é projetado, simulado e caracterizado na plataforma X-cut Lithium Niobate-On-Insulator (LNOI). Foi comprovando pela segunda vez que o LNOI é uma plataforma versátil capaz de permitir a Integração de AWG. As restrições e otimizações necessárias foram analisadas para poder desenvolver um AWG de maior desempenho nesta plataforma. Aqui, são apresentadas simulações informando sobre a física do dispositivo e os parâmetros cruciais do projeto. Foi demonstrado um AWG 9x9 funcional em LNOI X-cut para a banda óptica C, com espaçamento entre canais de 0,9 nm e perda de inserção de 21 dB.

Palavras-chave: Arrayed Waveguide Grating, Região de Propagação Livre, Dispositivos Ópticos Integrados, Lithium Niobate-On-Insulator, Phased Array, Rowland Circle.

Contents

List of Figures

List of Tables

Acronyms

AWG Arrayed Waveguide Grating *(pp. 1–5, 7–12, 16–23, 26, 29–31)*

BB Building Block *(pp. 2, 5, 29, 31)*

CMOS Complementary Metal Oxide Semiconductor *(p. 13)*

deMUX Demultiplexing *(pp. 8, 26)*

EME Lumerical's EigenMode Expansion solver *(p. 16)*

FDTD Finite-Difference Time-Domain *(p. 17)*
FIB Focused Ion Beam *(p. 14)*
FPR Free Propagation Region *(pp. 4, 10–12, 16–24, 27, 29–31)*
FSR Free Spectral Range *(pp. 8, 12, 18, 25)*

ICP-RIE Inductively Coupled Plasma Reactive Ion Etching *(p. 14)*

LNO Lithium Niobate *(pp. 1, 2, 4, 12–14, 16, 17)*
LNOI Lithium Niobate-On-Insulator *(pp. 1–3, 5, 14–16, 19, 24, 25, 29–31)*

MMI Multimode Interferometer *(pp. 18, 30)*
MUX Multiplexing *(pp. 8, 26)*
MZI Mach-Zehnder Interferometer *(pp. 18, 30)*
MZM Mach-Zehnder modulator *(pp. 5, 15)*

OSA Optical Spectrum Analyzer *(p. 18)*

PHASAR Phased Array of waveguides *(pp. 10, 18, 19, 21, 23, 25, 27, 29, 30)*
PIC Photonic Integrated Circuits *(pp. 15, 18)*

PLACE Photolithography-Assisted Chemo-mechanical Etching *(p. 14)*

RC Rowland Circle *(pp. 10, 17, 27, 31)*
RIE Reactive-Ion Etching *(pp. 1, 14)*

SLED Superluminescent diode *(p. 18)*
SOI Silicon-On-Insulator *(pp. 1, 2, 14)*

TE Transverse Electric *(p. 16)*

varFDTD Lumerical's 2.5D variational Finite-Difference Time-Domain *(p. 17)*

Symbols

β	Phase constant *(p. 7)*
$\Delta\lambda_{3dB}$	The 3 dB channel Bandwidth in terms of wavelength *(p. 9)*
$\Delta\upsilon_{3dB}$	The 3 dB channel Bandwidth in terms of frequency *(p. 9)*
D	Dispersion inside the Rowland Circle *(p. 12)*
d_a	Spacing between adjacent arrayed waveguides *(pp. 11, 21)*
ΔL	Path length difference between adjacent arrayed waveguides *(pp. 10, 11, 18, 25, 27, 30)*
$\Delta\lambda_{ch}$	Channel Spacing in terms of wavelength *(pp. 8, 11)*
d_o	Spacing between adjacent receiver/output waveguides *(p. 21)*
$\Delta\theta$	Angular spacing between adjacent arrayed waveguides *(p. 11)*
$\Delta\upsilon_{ch}$	Channel Spacing in terms of frequency *(p. 8)*
$\Delta\lambda_{FSR}$	Free Spectral Range in terms of wavelength *(pp. 8, 12)*
$\Delta\upsilon_{FSR}$	Free Spectral Range in terms of frequency *(pp. 8, 12)*
IL_0	Insertion Loss of central channel *(pp. 8, 9)*
k	Propagation constant *(p. 7)*
λ_0	Wavelength of the central channel *(pp. 8, 11)*
L_u	The Loss of Non-uniformity *(p. 9)*
m	Diffrection order *(p. 11)*
N_a	Number of arrayed waveguides *(p. 21)*
n_{eff}	Effective refractive index *(p. 7)*
n_s	Effective refractive index of Slab region *(p. 11)*
n_w	Effective refractive index of waveguide region *(p. 11)*

n_g Group refractive index of waveguide region *(p. 11)*

π The numerical value of pi *(p. 10)*

R_a Focal length of the free propagation region *(p. 11)*

v The propagated frequency *(p. 7)*

v_0 Frequency of the central channel *(p. 8)*

$Xtlk$ Adjacent channel Crosstalk *(p. 9)*

1

Introduction

This thesis focused on the development of an Arrayed Waveguide Grating (AWG) on the Lithium Niobate-On-Insulator (LNOI) platform. In order to understand the physics and functionality of this device as well as its development process, this thesis was structured in the following manner: An Introduction to the AWG, first a look through literature and commercial devices, resulting in the motivation and objective for this thesis; Methods and Materials, beginning with a theoretical background of the AWG concept and the LNOI platform, and in addition a description of the procedure for developing this complex device; Afterwards the design model along with results from simulations and measurements is presented and fully discussed; In the last chapter a summary of this development process is presented together with the future perspectives on improving the AWG performance and versatility.

1.1 State of the Art

In order to better understand the AWG device performance, as well as the LNOI platform technology, a review of the literature is essential, it also provides the description of the multiple challenges, constraints and achievements noted to this date.

The electro-optic properties of Lithium Niobate (LNO), especially its strong pockels effect, make it the right material for photonic applications. This material is even often referred to as the silicon in photonic applications. The improvements in fabrication have allowed for the implementation of a variety of devices in LNOI technology. LNOI structure is similar to that of Silicon-On-Insulator (SOI) technologies. However, its fabrication is more complex than that of SOI. The etching of such substrate can be done in two fashions, either dry or wet etching. While wet etching is a simpler and faster method, with high etching rates, it is also less reliable, reproducible and with lower resolution, [28]. Therefore, for integrated optics, a variety of dry etching techniques can be applied [46]. A very common one is Reactive-Ion Etching (RIE), [46, 4, 24]. Although RIE is a scalable and reliable technique for such applications, it is impossible to have a perfect etching on the sides of the waveguides, leaving them at a certain angle. Depending on the etching

process, as well as the crystallographic axes on which the etching occurs, this angle, of the waveguide wall, will differ, [24, 46].

To improve such technology a crucial step is the optimization of waveguide fabrication, with the intention of achieving low losses and small bending radii. Two common implemented waveguide structures are wire, ridge and rib configurations. Wire waveguides allow for smaller bending radii, while rib structures ensure less loss since the light mode is not as close to the waveguide walls, [7, 43]. In rib waveguides, losses below 1 dB per centimetre have already been demonstrated, [55]. The LNO waveguide sidewall angle that results from the etching process contrasts with the waveguide sidewalls found on silicon technologies, that are close to vertical, this can come as a constraint for the development of certain devices in LNO, [30].

A variety of devices have already been developed and optimized in the LNOI platform, such as racetrack Modulators, [35], waveguide Bragg gratings, [39], spectometers, [40], supercontinuum light generation, [15], multimode interferometers, [57], Mach Zehnder interferometer modulators, [20], among other couplers and devices.

The Arrayed Waveguide Grating full model was firstly described by Smit, in 1996, as a PHASAR (phased array), [47]. The deployment of such device in a variety of technologies has been extensive, and it is expected to be an even more important Building Block (BB) for integrated sensors and telecommunications.

Such a device has been shown and optimized in a variety of material platforms. SOI platform is highly used and has been used for a variety of applications for the C-band and in other optical bands. Other materials typically used are Silicon Nitrite and silica-based waveguides. In relation to this thesis, it is important to look at typical performance values in literature, so as to know what values to strive for. For the design application, the most important performance results to analyse are the Insertion loss and Crosstalk between adjacent channels. Silicon on Insulator platform is typically used for the implementation of such a device as an AWG. Common values for insertion loss are around 3 dB and below -20 dB crosstalk, [25, 54], as observed in figure, 1.1.

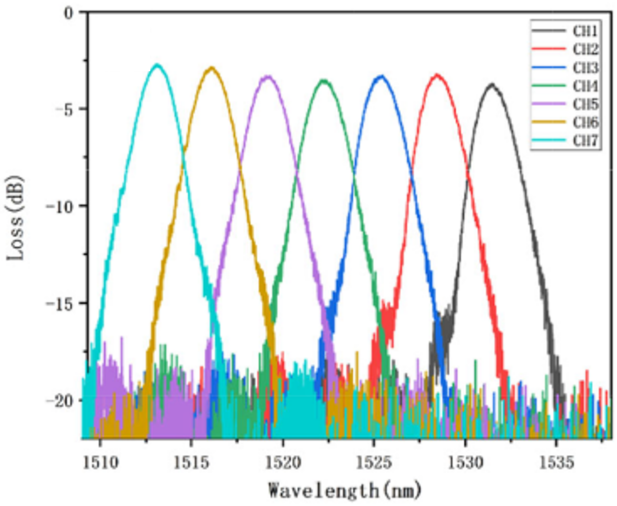

Figure 1.1: Spectrum of AWG on Si, with 100 GHz channel spacing. Adopted from [54].

In Silicon Nitride technologies common values are also reported, [19], figure 1.2, or even with losses below 2dB, [45].

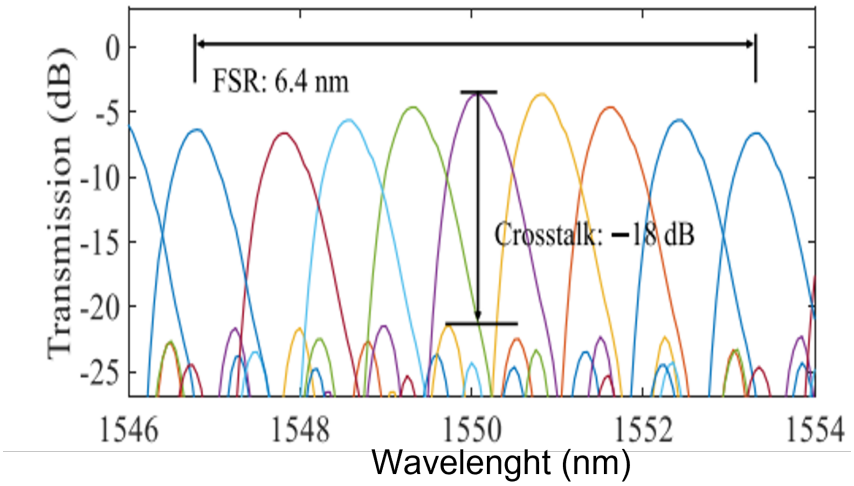

Figure 1.2: Spectrum of AWG on Si_3N_4, with 100 GHz channel spacing. Adopted from [19].

In commercial products, the optical insertion loss is slightly higher, around 4dB. However, that loss already takes to account the packaging coupling. In regards to crosstalk, there is typically an optimization, with common crosstalk values of -25dB, [13, 2, 16].

In contrast to the extensive application of this device in these material platforms, the implementation of AWG in LNOI has been close to null, with only one exemplar found in the literature, up to date. In 2018, Ben Yoo et al. implemented the AWG on LNOI, Z-cut, platform, with 8 channels of a 500 GHz spacing, with a rib waveguide of 2 μm width. The experimental results present very different values compared to the previous technologies,

insertion loss of 25 dB and crosstalk of -15dB, [59], as can be observed in figure 1.3. It is then important to research this device in this platform to better understand the constraint and limitations in contrast to currently material platforms.

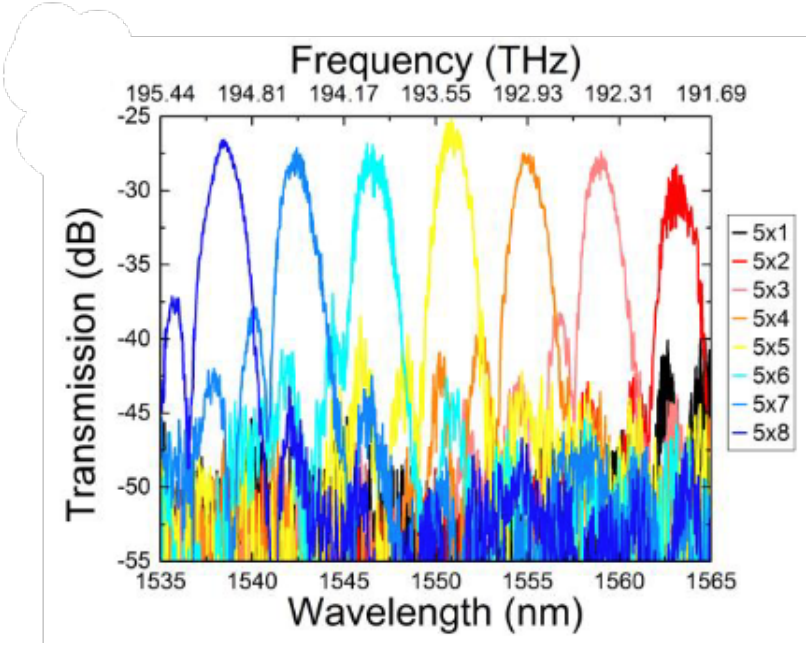

Figure 1.3: Spectrum of AWG on Z-cut LNOI, with 500 GHz channel spacing. Adopted from [59].

Due to fabrication mismatch and environmental conditions, such as temperature and vibrations, the AWG central wavelength can shift from the design, and consequently all the channels' wavelengths. Common strategies for tuning the central wavelength are the usage of a thermal actuator to control the operational temperature, [58], or to vary the refractive index in the arrayed waveguides using the thermal-optic or electro-optic effect, [3]. Since LNO has very remarkable electro-optic properties, the tunability of the central waveguide by the electro-optical effect is a promising strategy, as was already simulated, [27], with a tuning range of 4 nm.

A variety of structures have also been implemented in conjunction with the AWG so to improve performance or control the shape of each channel, such as for decreasing reflection inside the Free Propagation Region (FPR), [10], or decreasing the loss between the arrayed waveguides and the FPR by tapering the waveguides in a variety of fashions, either vertically, [49], by using multimode interferometers at that interface, [33], or common waveguide tapering, [37].

1.2 Motivation and objectives

Telecommunications is a technology field that has been expanding swiftly in the last century. In 1965, Charles Kao studied clear glass fibres to be a viable telecommunication medium, [22] and from then on Telecom data transfer is established primarily with

optic fibre. Therefore an array of photonic structures have been developed to date. The increasing demand for better performance has created a continuous desideratum for the investigation and optimization of this field. In the era of a globalized civilization, the field of telecommunications is surely expected to grow and achieve even more complexity than nowadays. Future advancements in this communication field are based on the increasing demand for faster and more capable telecommunication technologies. Therefore, the development of photonic devices' bandwidth and speed capacity is a necessity, so to enable more efficient communication. These structures constitute a set of functions that allow the optical signal to be received, modulated and transmitted, [44].

Therefore, this project aimed to strive forward and develop an AWG structure in the Lithium Niobate-on-Insulator platform, in LNOI X-cut. This device can have several applications, the application for which it was designed is a high-speed transmitter, composed of an AWG as a demultiplexing stage, where each of the channels would be coupled to a Mach-Zehnder modulator (MZM) of 100 Gbit/s data modulation speeds, these modulated signals would then be focused onto a single output fibre with an AWG acting as a multiplexing stage, as represented in the sketch of figure 1.4. This application idea forced the selection for the LNOI X-cut, given the stronger modulation when the MZM electrodes are designed in a way that the electric field generated is aligned with the extraordinary refractive index of the Lithium Niobate.

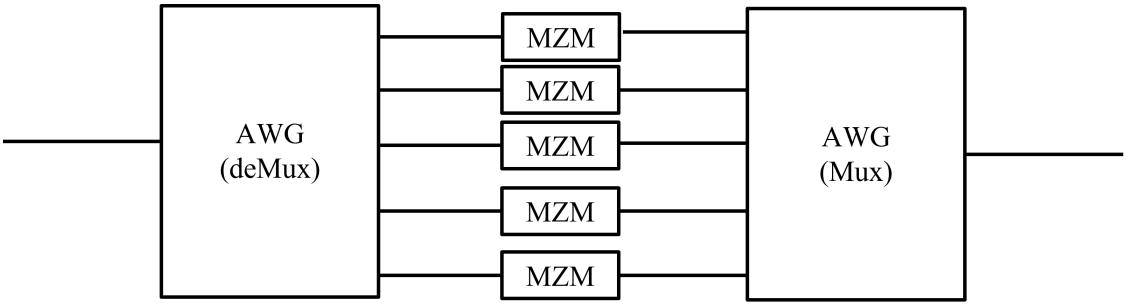

Figure 1.4: AWG+MZM+AWG High-speed Transceiver.

The AWG is a fairly new device in the LNOI platform, with only one published exemplar, [59]. Therefore the development of this device is another step in assessing the capability and versatility of the LNOI platform. In addition, it is also a new passive optical BB for Versics and for the Optical Nanomaterial group at ETH.

2

Methods and Materials

2.1 Theoretical Background

In this section the AWG will be fully explained, the physical concept behind this optical device, the modeling of such a device, its functionality and preformance. Further the LNOI platform will be discribed and analyzed.

2.1.1 AWG Theory

The way to confine and distribute light in photonic integrated circuits is through the use of waveguides. Light confined in these structures is propagated throughout modes, this refers to the distribution of optical power through the waveguide. This mode depends on the material's refractive index, the waveguide dimensions and structure, and propagated frequency. A rib waveguide structure is composed of a cladding layer and a core consisting of a thin film layer and a strip waveguide of the same material. This architecture allows for better confinement of the propagated light signal in contrast with strip waveguides.

The effective refractive index (n_{eff}), of a certain mode at a specific frequency, can be given by equation 2.1. Where β is the phase constant, k is the propagation constant and v the propagated frequency.

$$n_{eff} = \frac{\beta}{k} = \frac{c}{v} \tag{2.1}$$

The effective refractive index that the light mode will experience, for a specific frequency, inside the waveguide will not depend solely on the refractive index of the core material but also on the cladding and on the waveguide structure itself. Therefore, the best strategy for calculating the effective refractive index in a rib waveguide configuration is through simulation. In a slab region, the width is much larger compared with the thickness of the rib structure. Therefore the effective refractive index is dependent only on the thickness of that structure, analogously to a planar waveguide configuration, [21].

Wavelength Division Multiplexing is a common methodology to enhance the capacity of a fibre network, allowing the encoding of multiple wavelength channels into a single fibre or waveguide. The AWG is a device capable of achieving that, through multiplexing

and demultiplexing. The Multiplexing (MUX) aspect allows for the encoding of multiple wavelengths at a single output channel. In the opposite fashion, it is also capable of Demultiplexing (deMUX) a complex signal, separating it into a set of wavelength channels, figure 2.1.

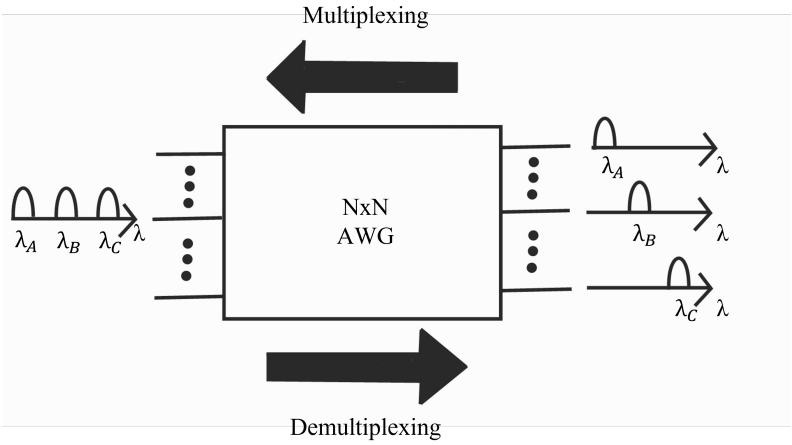

Figure 2.1: AWG MUX and deMUX procedure.

Being a bidirectional device capable of MUX and deMUX, it has a cyclic behaviour, depending on the excited input port each wavelength channel will be read at a different output port, figure 2.2. For example, in a deMUX configuration, if a signal is applied at the centre input port, the central wavelength channel will appear at the central output port. However, if the input port is shifted, the central channel will appear at a different output port, [8, 18, 1].

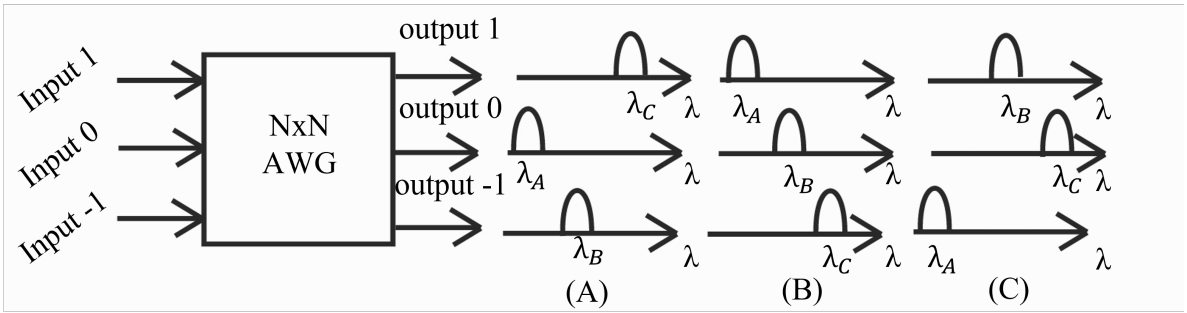

Figure 2.2: AWG routing, (A) Input 1, (B) Input 0, (C) Input -1.

Apart from the functionality of the device, the performance focuses on a set of parameters. Important parameters set in modelling of the AWG are the wavelength or frequency of the Central Channel ($\lambda_0 \mid \upsilon_0$) and the spacing between channels, Channel Spacing ($\Delta\lambda_{ch} \mid \Delta\upsilon_{ch}$). Given that the AWG spectra is periodic, that periodicity is referred as Free Spectral Range (FSR), ($\Delta\lambda_{FSR} \mid \Delta\upsilon_{FSR}$). The Insertion Loss ($IL_0$) is the loss of signal intensity from the whole device and the isolation of channels is considered the adjacent channel Crosstalk

($Xtlk$). In regard to the spectral shape, there is the 3 dB Bandwidth ($\Delta\lambda_{3dB}$ | $\Delta\upsilon_{3dB}$), the width of the channel at a transmission of $IL_0 - 3dB$. The Loss of Non-uniformity (L_u) is the difference in Insertion Loss from the central channel to a channel at the extremity.

Table 2.1: AWG Performance Parameters nomenclature.

Performance Parameter	Symbol	Units
Central Channel	λ_0 υ_0	nm THz
Channel Spacing	$\Delta\lambda_{ch}$	nm
Free Spectral Range	$\Delta\lambda_{FSR}$ $\Delta\upsilon_{FSR}$	nm GHz
Channel bandwidth 3dB	$\Delta\lambda_{3dB}$ $\Delta\upsilon_{3dB}$	nm GHz
Insertion Loss of the Central Channel	IL_0	dB
Loss of non-uniformity	L_u	dB
Crosstalk between adjacent channels	$Xtlk$	dB

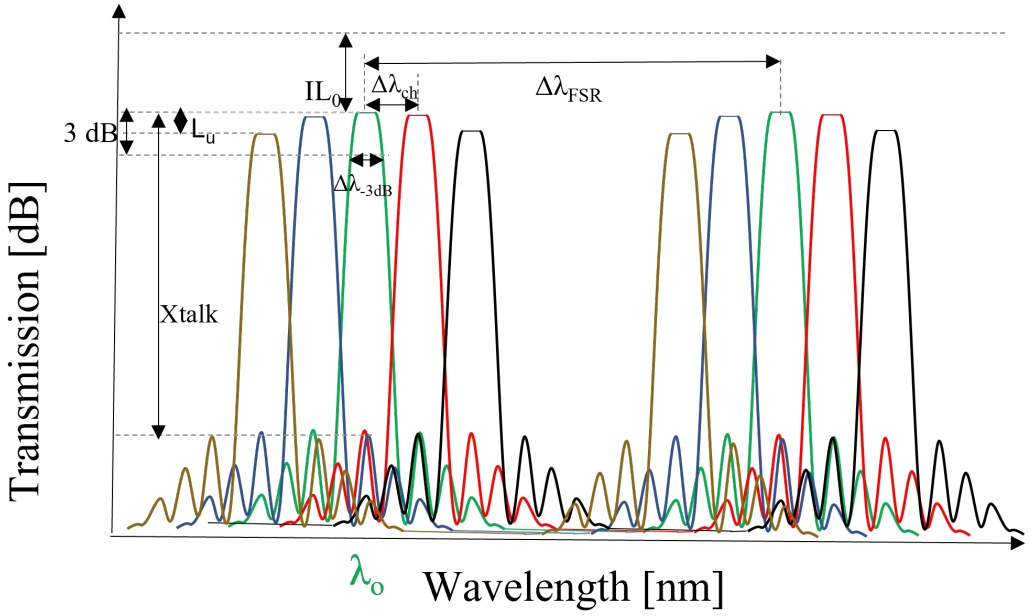

Figure 2.3: AWG performance parameters.

The AWG is a complex device, and so the modelling of such a device is intricate. Many approaches have been taken into account, the Smit model description which [47], focuses on the designed parameters is a typical model to follow. Other models focus on designing the AWG from the required performance, [36, 9]. Focusing on the Smit model, [47], the design is grounded on a set of initial key parameter specifications that need to be selected. These are the number of channels, the central frequency and channel

spacing, the ideal 3-dB bandwidth, the ideal maximal insertion loss, the maximal loss of non-uniformity tolerated and the ideal maximal adjacent crosstalk level. From there, the design dimensions of the AWG can be determined. In order to understand the role of each parameter in the design, a theoretical background should be first comprehended.

The AWG is composed of two slab structures or two FPR connected by a Phased Array of waveguides (PHASAR), figure 2.4 A. The FPR can have different star coupler configurations, the most common ones are the Confocal configuration, [12], or the Rowland Circle (RC), [34]. The confocal configuration is designed as a typical confocal lens where the interfaces of the slab with the array or the receiver/output waveguides have the same curvature [62]. In the RC the array waveguides connect to the slab at a region with a curvature of a certain radius, being this radius the focal length of the RC, and the receiver/output waveguides connect at a curvature of half that radius, [53], as indicated in figure 2.4 B.

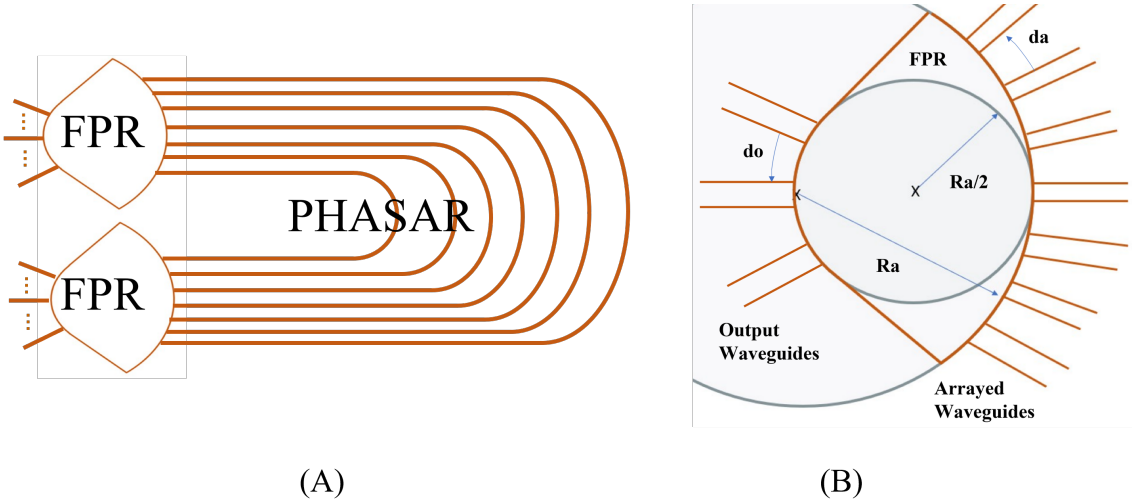

Figure 2.4: (A) AWG layout and constituent parts; (B) FPR Rowland Circle geometry.

The first AWG designs of this Thesis took into account the Confocal-type star coupler, later the Rowland Circle type was employed for better crosstalk, insertion loss and non-uniformity between channels performance, as concluded from the literature, [62]. When the light signal is input at the first FPR, with an angle θ_{in}, it diffracts throughout the FPR. Due to the design of the FPR structure, based on the Rowland Circle, the signal is focused and uniformly illuminated at each arrayed waveguide, figure 2.5. The signal is then illuminated throughout each arrayed waveguide. The waveguides of the array differ in path length, in a way that each waveguide has a length difference of ΔL to the adjacent ones. This path length difference creates a 2π phase shift between adjacent waveguides. This phase shift induced in the arrayed waveguides results in an interference pattern at the second FPR, so that there will be positive interference at certain spatial regions, correspondent to the output waveguides, where light is propagated with an angle of θ_{out}.

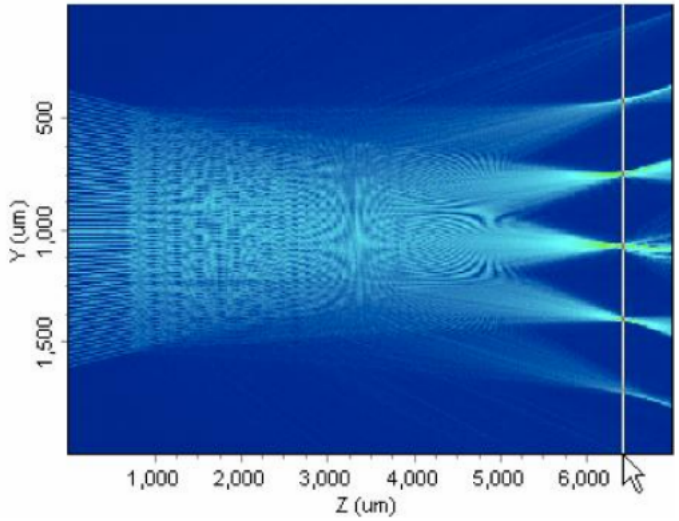

Figure 2.5: FPR interference focusing at each output channel. Adopted from [6].

This way the input signal can be routed to the multiple output waveguide and centred at a particular frequency channel at each output port, acting as a demultiplexing stage. Given that the AWG is a bidirectional passive optical device, it can function as a multiplexer or demultiplexer stage.

The full illumination pathway is described in the following equation:

$$n_s d_a sin(\theta_{in}) + n_w \Delta L + n_s d_a sin(\theta_{out}) = m\lambda_0 \tag{2.2}$$

Having n_w and n_s as the effective refractive indexes of both the array waveguides and the FPR, respectively; the m is the diffraction order; λ_0 is the propagated wavelength and d_a as the spacing between adjacent arrayed waveguides. From equation 2.2, path length difference (ΔL) and angular spacing ($\Delta\theta$) can be derived for adjacent arrayed waveguides.

In addition, the focal length (R_a) of the FPR, or slab, can be obtained, being equal to the grating circle radius (radius of the curvature at the array interference) and twice the Rowland circle radius. These equations are derived as follows:

$$\Delta L = \frac{m \cdot \lambda_0}{n_w} \tag{2.3}$$

$$\Delta\theta = \frac{n_g}{n_w} \frac{m \cdot \Delta\lambda_{ch}}{n_s d_a} \tag{2.4}$$

$$R_a = \frac{n_w}{n_g} \frac{n_s d_a^2}{m \cdot \Delta\lambda_{ch}} \tag{2.5}$$

With n_g referring to the group refractive index of the array waveguides, given by $n_w - \lambda_0 \frac{d_a n_w}{\Delta\lambda_{ch}}$.

Although the AWG channels are designed at a certain wavelength or frequency, they will appear periodically throughout the spectrum. such wavelength period is referred to

as FSR, it can be given in terms of wavelength ($\Delta\lambda_{FSR}$) or frequency ($\Delta\upsilon_{FSR}$), expressed in the equation 2.6.

$$\Delta\upsilon_{FSR} = \frac{c}{n_g \Delta L} \tag{2.6}$$

The dispersion (D) of the FPR can be given as follows:

$$D = \frac{1}{\upsilon_0}\frac{n_g}{n_s}\frac{\Delta L \cdot R_a}{d_a} \tag{2.7}$$

These equations were fully described in the Smit model, [47], that has become the standard theoretical model for AWG thechnologies. The AWG losses result from multiple phenomena in the light path. One of the most critical is the interface between each FPR and the array waveguides, given the discontinuity in the mode field present at that interface. To prevent loss at this stage the arrayed waveguide spacing should be small and the transition from FPR to each waveguide should be continuous, so as not to have high contrast in mode volume. This is of course limited due to fabrication. To decrease the insertion loss at this stage, as well as increase crosstalk performance, the mode transition from FPR to each waveguide must be smoothed out. To achieve this, the usage of an etched taper at each array waveguide interface with an FPR can be applied, [37, 48]. The loss of the device also increased due to attenuation throughout the FPR.

2.1.2 Lithium Niobate-on-Insulator platform

Lithium Niobate ($LiNbO_3$) is a novel material, auspicious for integrated optic platforms. It is an inorganic, dielectric, ferroelectric material, that has proven to be very remarkable for photonic applications, due to its excellent electro-optic properties. Relevant properties are its strong second-order nonlinearity and negligible third-order nonlinearity, which allow for pure phase modulation with no absorption at a wide transmission spectrum (0.33 to 5.20 μm), [51]. LNO displays a trigonal crystal structure, lacking inversion symmetry, figure 2.6 (A). This structure implies nonlinear optical polarizability and susceptibility to the Pockels effect. Then, due to its birefringence and tensor electro-optic coefficient lithium niobate devices are polarization-dependent. The birefringence caused by the crystallographic structure of LNO results in an ordinary refractive index in x and y crystallographic direction, and an extraordinary refractive index in the z direction, smaller than the ordinary index, figure 2.6 (B), [14].

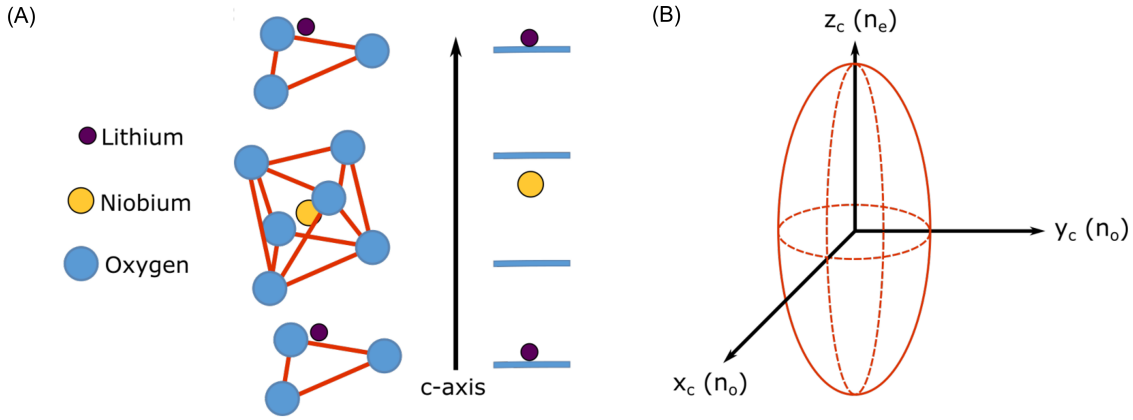

Figure 2.6: (A) Ferroelectric crystal structure of LNO, (B) Index ellipsoid of LNO. Adopted from [14].

The effect of this present birefringence can be visualized through out the wavelength spectrum in figure 2.7.

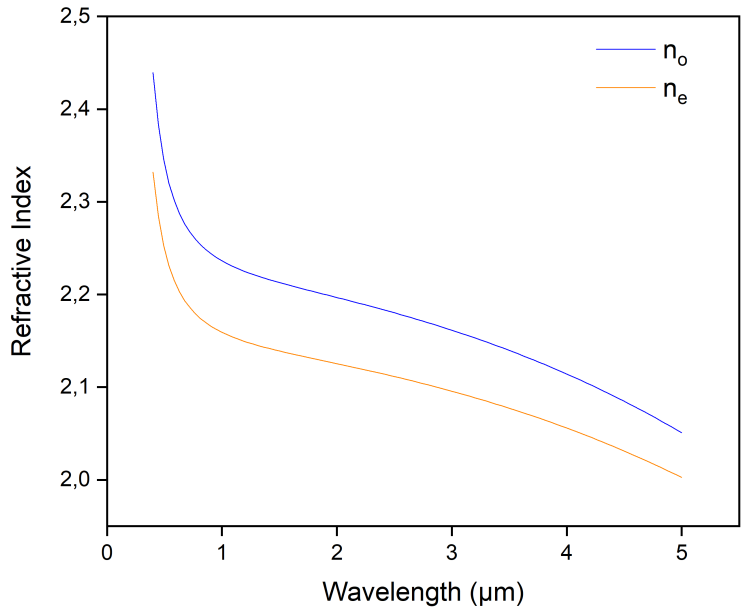

Figure 2.7: Ordinary n_o and Extraordinary n_e refractive index variance through out the light spectrum.

In bulk LNO modulators there is typically weak confinement. This implies electrode structures optimized for decreasing metal-related absorption losses, which increases the half-wave voltage to Complementary Metal Oxide Semiconductor (CMOS) non-compatible values, [17, 27, 11]. With the development of thin-film lithium niobate in the 2000s,[41, 50], this challenge was surpassed, due to the increase in waveguide confinement strength, [57,

30]. In resemblance to SOI, lithium niobate is often used in a similar structure, Lithium Niobate-On-Insulator, combining the material properties of LNO with the improvements of thin-film technology. This platform allows for high-performance compact modulators. LNOI can be fabricated by different methods, process optimization is still a big area of study. Etching is a common approach. In contrast to wet etching, dry etching' higher anisotropy provides more fabrication control, [30, 5]. Common etching techniques employed are RIE,[23, 52], often associated with high scattering losses, Photolithography-Assisted Chemo-mechanical Etching (PLACE), [60] and electron beam lithography, [38, 7]. Other fabrication techniques are based on ion bombardment, such as Focused Ion Beam (FIB) milling, [31], and the particular Argon ion milling, [29]. In FIB only low fabrication efficiency is available.

The developed process that supported this thesis incorporated the deposition of a hard mask, made from e-beam resist and thin films of chromium (Cr) and Silicon Oxide (SiO_x), that provide sufficient protection of the LNO and improve mask selectivity. the e-beam resist will be patterned, and after the dry etching of the thin film layers of Cr and SiO_x, the LNO can be etched safely. This etching was done by Inductively Coupled Plasma Reactive Ion Etching (ICP-RIE). The mask is then fully removed and the sample cleaned, figure 2.8, [14].

In LNO devices microcavities and waveguides act as building blocks that enable the construction of a wide range of photonic devices. The waveguide is a key part on the device optimization if low optical loss and high modulation efficiency are intended, [20].

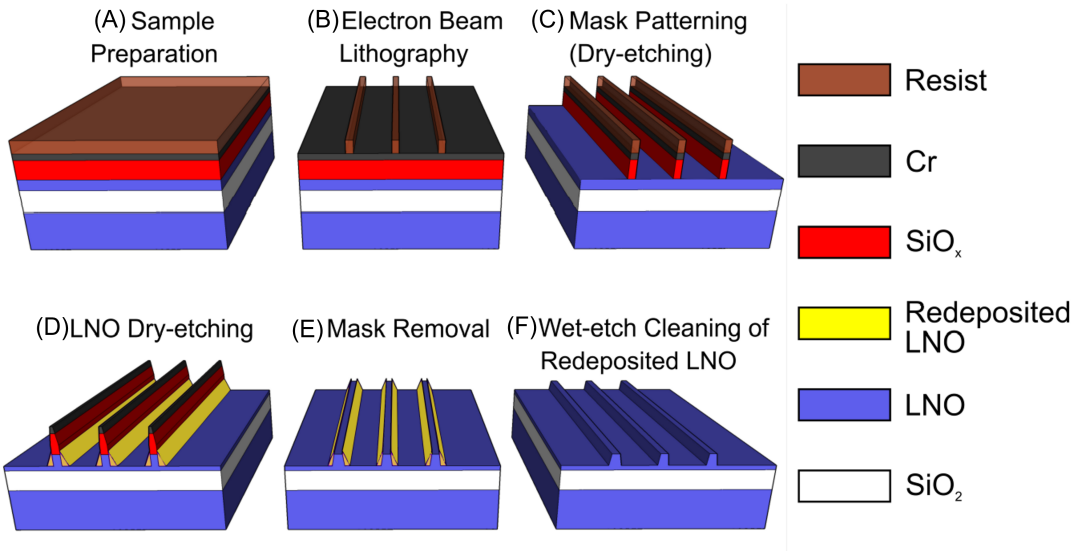

Figure 2.8: Fabrication procedure of LNO nanophotonic structures. (A) deposition of the mask, multi-layer structure of e-beam resist and a double film of chromium (Cr) and silicon oxide (SiO_X); (B) e-beam writing on the e-beam resist; (C) development and patterning of the mark by ICP-RIE; (D) LNO etching by ICP-RIE; (E) full mask removal; (F) sample cleaning. Adopted from [14].

LNOI Photonic Integrated Circuits (PIC) allow for an optimized simultaneous implementation of the multiple functional devices discussed above, [7, 61]. It is considered a novel material and much research are needed for improving the fabrication process and the consequent possible set of building blocks to be implemented. It sure is a promising material that has been proving critical in achieving better performances of certain photonic applications, [30], such as: Multimode Interferometer, [35, 56]; Mach-Zehnder Modulator, [20]; Bragg Gratings, [39]; and a variety of other devices. Only future research will tell the real limitations of such technology.

From the fabrication and cutting process, LNOI wafers are typically X-cut or Z-cut, regarding the crystallographic structure. In this project, X-cut wafers were used so to have both ordinary and extraordinary refractive indexes in the writing plane. This is important since aligning the electric field of the MZM with the extraordinary refractive index of the mode in the waveguide allows for a stronger and more efficient modulation, driving the π) voltage (V_π) down.

2.2 Methods

When discussing optical communication, the dependence of attenuation on the wavelength has to be acknowledged. Attenuation is the loss of signal throughout the transmission, limiting the length at which transmission can be possible. The Attenuation is driven by absorption and scattering, both effects depend on the transmitted wavelength. Absorption of ultra-violet, visible and infrared is present in the optical fibre material due to the excitation of the atoms and their electrons from the light stimulus. Scattering is due to diffuse reflection inside the fibre or waveguide. Therefore, for telecom, the C band (1530 to 1565 nm) is a common choice, [42]. In figure 2.9 it is possible to verify a lower range of attenuation correspondent to the optical C band. For the AWG device to be applicable to the market, the choice of central frequency was 192.1 THz, or 1560.6 nm, in terms of wavelength.

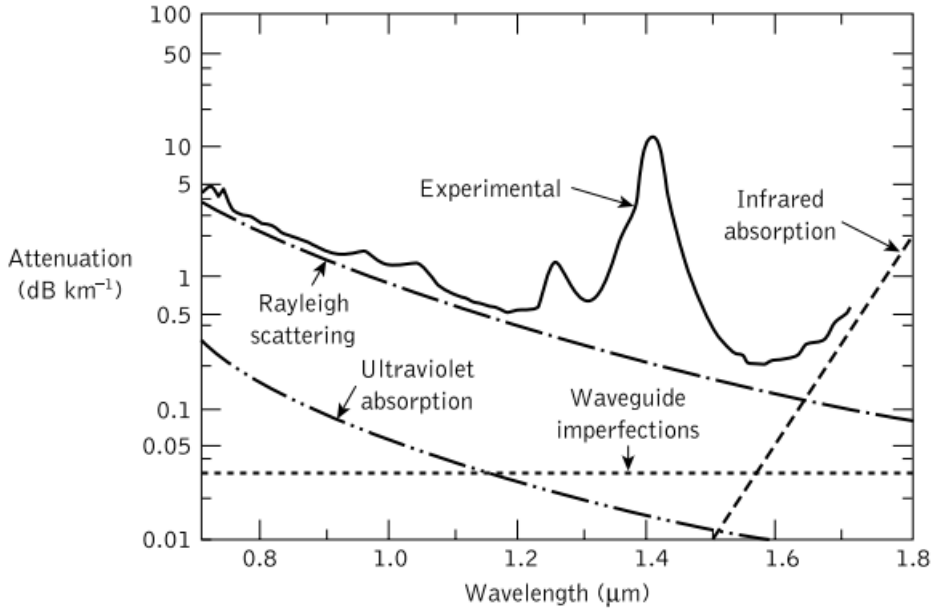

Figure 2.9: Ultra-low-loss single-mode fiber' measured attenuation spectrum, [42]

The first step for designing an AWG structure is to calculate the effective refractive index of the waveguides and FPR at the wavelength of the central channel, this calculation was done through simulation in Lumerical EigenMode Expansion solver (Lumerical's EigenMode Expansion solver (EME)). To induce this light propagation through the waveguides and slab region, a source of frequency of 192.1 THz, equivalent to the central frequency of the AWG designed response, was applied and the fundamental Transverse Electric (TE) mode was propagated. The effect of the bending of the waveguides on the propagation was also studied to have information in that regard for the design process.

The simulations and AWG designs are based on a LNOI structure of a 300 nm thin-film of LNO over a 2 μm glass film. The waveguides were of 1 μm with a 300 nm thickness, having a sidewall angle of 60°, resulting from the etching process. This structure is represented in figure 2.10.

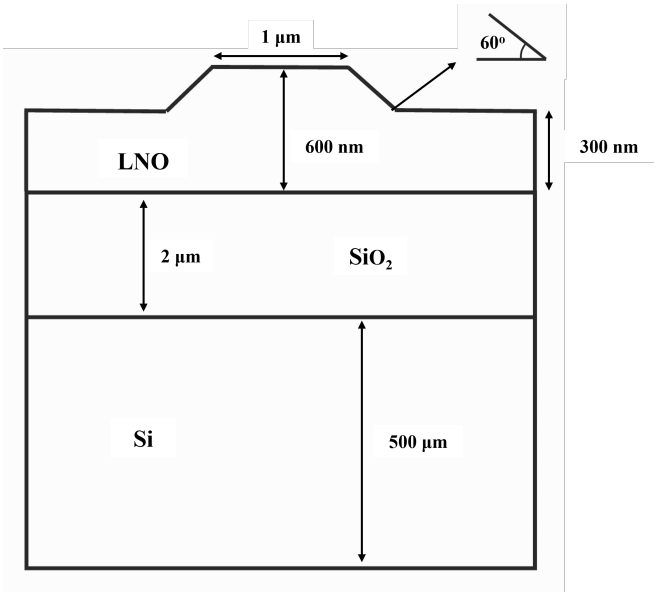

Figure 2.10: LNOI waveguide structure.

Having the effective index of the waveguides and slab regions the design followed the equations presented in the theoretical background section and the Smit model, [47].

Having the AWG and the FPR RC modeled, through a python script, based on the Smit model [47], that was able to calculate the design parameters of the AWG and draw its structure, or a single FPR on to a gds, using Nazca photonics. A set of simulations on the Lumerical Interconnect AWG module were carried out, by sweeping the design parameters such as the number of arrayed waveguides, arrayed and receiver/output waveguides spacing, with the intention of understanding the effect of these parameters on performance. In addition to these parameters, the AWG module also enables to specify the focal length and the order, that was adapted for each sweep point, based on the previously referred design parameters. From these simulations, the performance values were gathered and analysed. All simulation data analysis was carried by a python script design to extract the performance parameters with ease and to allow for a visual correlation of the design parameters onto preformance.

After gathering a more rich knowledge of the AWG, the device design was adapted. Then, in order to fully understand the focusing behaviour of the FPR, simulations of the already designed RC were carried out in Lumerical Lumerical's 2.5D variational Finite-Difference Time-Domain (varFDTD) software. Being Finite-Difference Time-Domain (FDTD) methods, where the time-dependent Maxwell's equations are calculated based on a finite central difference aproximation, the varFDTD (2.5D FDTD) is a faster simulation method compared 3D FDTD simulations. Here 2D simulations are carried out all along an axis where the model change of propagation can be ignored. Therefore making it a very fast and accurate method of omni-directional propagation. However, Lumerical varFDTD does not perform under birefringent materials, so only the ordinary refractive index of the LNO was taken into account.

After such simulations, the AWG was ready to be fabricated to then measure its response. The architectural gds design of this building block was written using Python and Nazca Photonics. At the end of the design, KLayout was used to merge all structures and to check the architectural design, to then be submitted for fabrication. The submitted chip was and integration of multiple device structures: Free Propagation Regions, where the design parameters were swept; imbalanced Mach-Zehnder Interferometer (MZI), where the fabricated path length difference could be studied; Full AWG, where the same sweep of design parameters was applied. This sectioning allowed for the verification of each AWG constituent, FPR and PHASAR, as well as the full integrated device. An imbalanced MZI composed of a set of two Multimode Interferometer (MMI) coupled to a pair of consequent waveguides, similar to a set of two arrayed waveguides of the AWG, surged as a strategy for measuring indirectly the path length difference (ΔL) of the PHASAR region. The MZI will have a filtering behaviour with a certain periodicity, the FSR. Here FSR is correlated to the ΔL responsible for the imbalance between both arms of the MZI, this relation is given by equation 2.6.

The fabricated AWG were also simulated using the interconnect module to be compared with the measured response.

The measurement set-up was a simple optical transmission configuration, having a Superluminescent diode (SLED), as a broadband source centred at a wavelength of 1550 nm, whose signal was transmitted through a lensed fibre and coupled onto the chip. The signal at the output of the PIC chip is then coupled onto another lensed fibre and the signal is transmitted to an Optical Spectrum Analyzer (OSA), OSA202C from Thorlabs. The lensed fibres are aligned and controlled by piezoelectric three-dimensional stages, as represented on figure 2.11.

From the measurements, it was possible to verify the functionality of the FPR and the PHASAR design. In regard to the AWG, it was possible to select a device whose response in terms of functionality and performance was clear and informative.

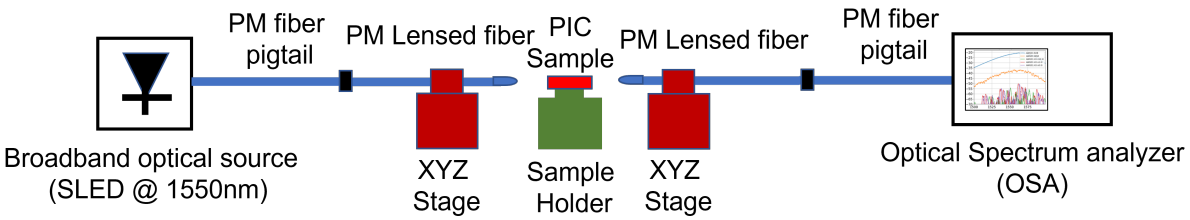

Figure 2.11: PIC transmission measurement set-up.

3

Results and Discussion

3.1 FPR and AWG design

The PHASAR component of the AWG can be designed in a variety of ways given that the path length difference is maintained, [26]. Two common designs are the conventional (round) shape, and the saddle shape, as seen in figure 3.1. In this thesis approach, the saddle shape was used for a future better control of the LNOI birefringence.

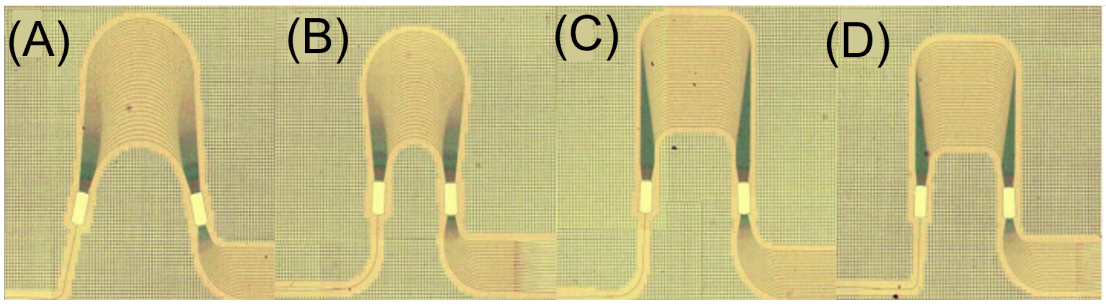

Figure 3.1: (A) and (B) Conventional AWG shape. (C) and (D) Saddle Shape. Adopted from [26].

The first step in designing the AWG was the calculation by simulations of the effective mode profile when light is propagated through the waveguides and the slab-like FPR.

In a slab region like the AWG free propagation region, the width and length dimensions are far greater compared to the thickness of the rib structure. In this way, the effective refractive index is mostly dependent on the thickness of the film.

From the simulations, it was possible to gather the effective refractive index of the waveguides and the FPR, with values of 1.91 and 1.97, respectively, for the centre wavelength, figure 3.2. In table 3.1, the effective and group indexes, and the effective mode area are presented for the waveguides and the FPR.

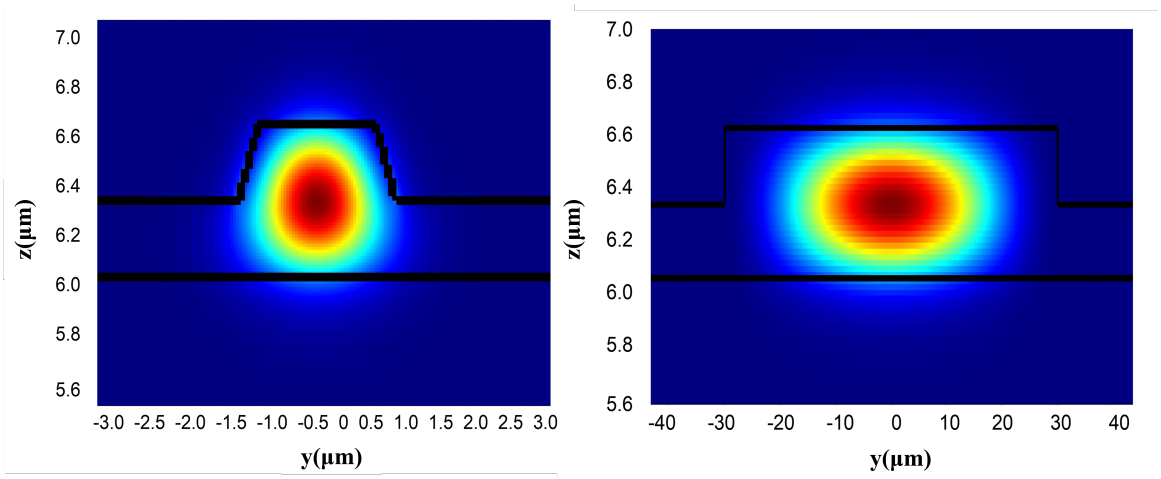

Figure 3.2: Mode profile simulation, (A) of the waveguide, (B) of the slab structure.

Table 3.1: Light Propagation Parameters for the Waveguides and FPR.

Parameter	Waveguide	FPR	Units
Effective Refractive Index (n_{eff})	1.910	1.966	–
Group Index (n_g)	2.265	2.232	–
Effective Mode Area	0.877	27.082	μm^2

3.2 varFDTD simulations

After the AWG design parameters have been calculated by the design model, the FPR was studied by varFDTD simulations, observed in figure 3.3, to ensure proper focus and arrayed waveguide confinement. It was possible to observe the broadening of the mode from the input waveguide all throughout the FPR. This dispersion would then be focused onto each arrayed waveguide. From the dispersion cone pattern, it is possible to verify the non-uniformity between the arrayed waveguides, where the central waveguides are able to couple more light, having more power intensity, than the arrayed waveguides on the extremities. The light is confined inside the arrayed waveguides, however, some light is transmitted also in the glass in-between the arrayed waveguides. This light transmission will have high attenuation, fading out throughout the glass. It was also possible to observe some reflection in the sidewalls of the FPR that would result in a certain interference pattern, affecting the focusing and lowering the AWG performance. This reflection was minimized with a slightly different design in the fabrication of the AWG chip, for measurements, even though, the effect on AWG performance should not be significant in this development stage.

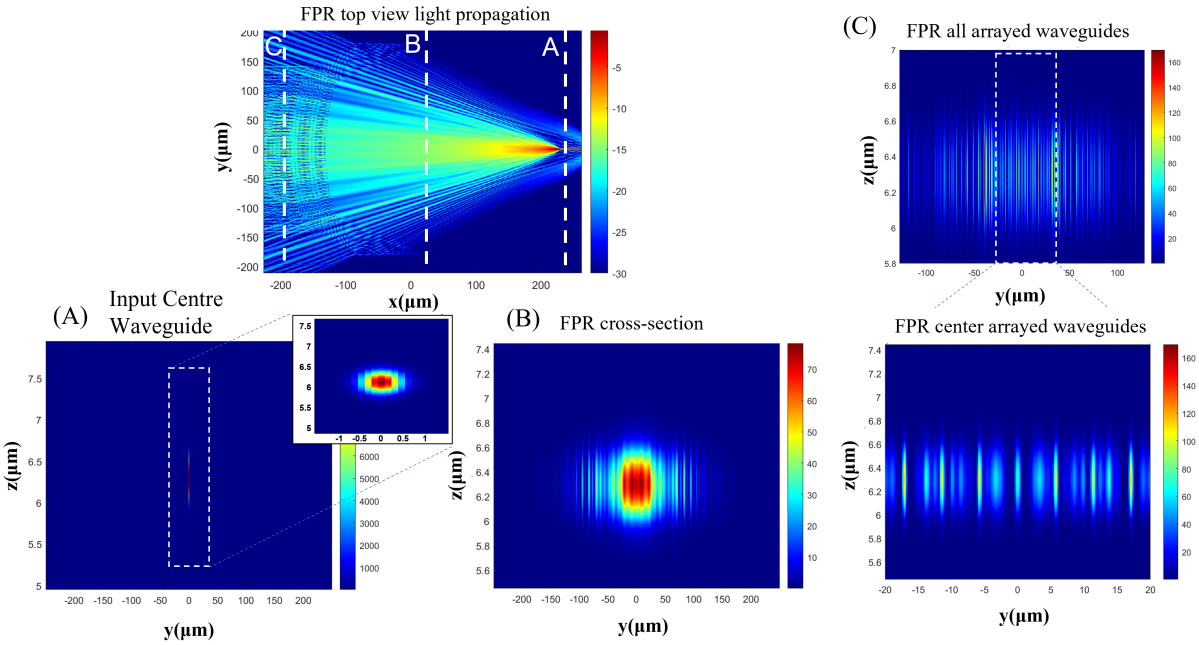

Figure 3.3: varFDTD FPR simulations. (A) monitor at input waveguide; (B) monitor at the mid-slab cross-section; (C) monitor at arrayed waveguides cross-section.

3.3 AWG interconnect simulations

The Interconnect simulations allowed to understand the role of each design parameter on performance, as well as the simulated response of a full AWG.

The insertion loss is the sum of a set of loss stages, three of the most crucial are the mode change in the interface between the FPR and the array waveguides, the propagation loss throughout the Slab region (FPR) and through the arrayed waveguides. In order to reduce the loss at the interface between the array and each FPR the mode variance should be as little as possible, this can be achieved by tapering the waveguides or using multi-mode waveguides. It is also important to minimize the reflections inside the slab, so the best strategy is to reduce the arrayed and output waveguides spacing, d_a and d_o respectively, to the minimum value allowed by fabrication, which will correspond to the lowest insertion loss. The number of arrayed waveguide (N_a) is also correlated to insertion loss performance given that this number must be sufficient to extract more light from the FPR slab to the PHASAR, minimizing reflection. However, a higher number of array waveguides will distort the signal resulting in a non-defined peak, the response spectrum will show less symmetric channels with additional roughness at the peaks, which is not tolerable for modulation, figure 3.4.

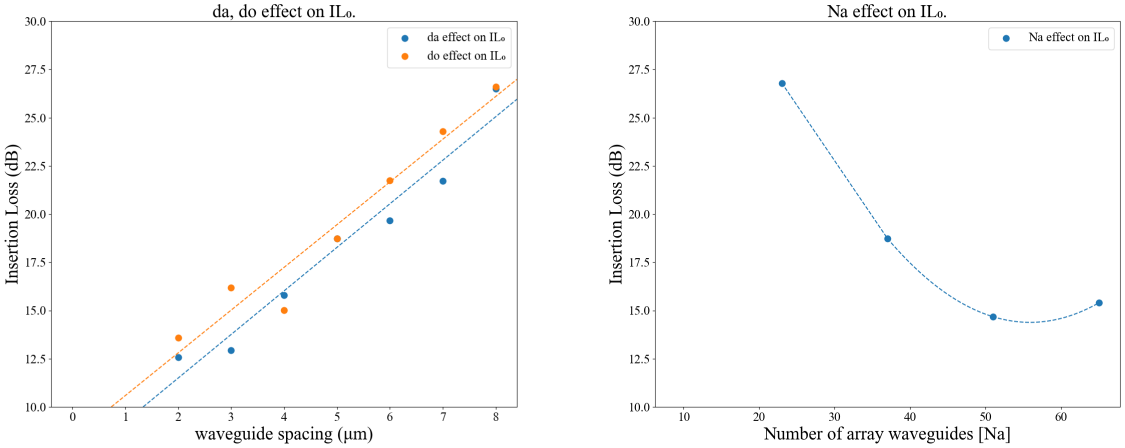

Figure 3.4: Simulated effect of design parameters on Insertion Loss (IL_0).

The crosstalk will be mostly given by the receiver/output waveguide spacing, given this parameter is correlated to the focal length of the FPR. Therefore, increasing this pitch up to a certain point will decrease crosstalk, figure 3.5.

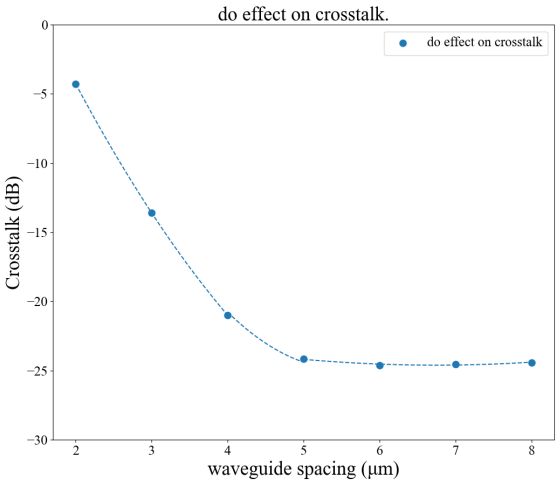

Figure 3.5: Simulated effect of design parameter on Adjacent Crosstalk (Xtlk).

The effect of the output spacing on the 3dB bandwidth of each channel tends to be the opposite, increasing this pitch will lower bandwidth. Therefore, a design choice has to be made regarding the relevance of both performance parameters, figure 3.6. In a more advanced stage, structural optimizations with tappers can also improve the channel shape to a flat-top AWG, increasing bandwidth while still achieving low crosstalk.

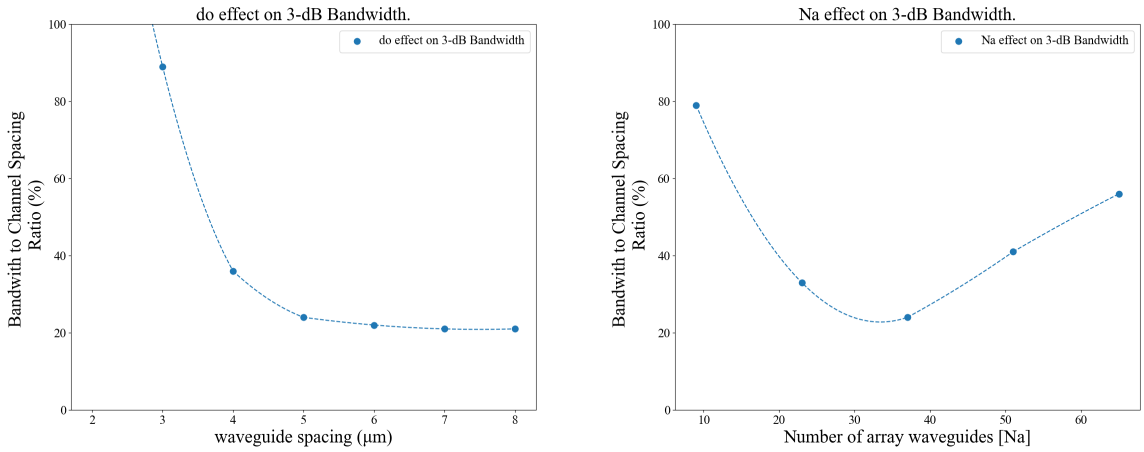

Figure 3.6: Simulated effect of design parameters on 3dB Bandwidth ($\Delta\lambda_{3dB}$ | $\Delta\upsilon_{3dB}$).

In order to have a comparison, in terms of performance, between the measured AWG and a theoretical approach, the simulations of three AWG designs, present in the fabrication of the AWG chip were carried out. One exemplar with the best-simulated performance fabricated on-chip (AWG 1), which its measurement was not clear, another AWG (AWG 2) whose response was also not clear, even though the FPR and PHASAR measurements, based on those parameters were valuable and a third AWG (AWG 3) with informative measurements in terms of functionality and performance. The design and performance parameter values are described in table 3.2

Table 3.2: AWG Interconnect Simulations.

Parameter	AWG 1	AWG 2	AWG 3	Units
Array waveguide spacing (d_a)	4	6	6	μm
Number of arrayed waveguides (N_a)	51	37	37	μm
Focal length (R_a)	360	360	420	μm
Path length difference in PHASAR (ΔL)	93	139	139	μm
Insertion loss (IL)	17.4	19.6	20.8	dB
Adjacent crosstlak ($Xtlk$)	−25.5	−25.0	−28.2	dB
3dB Bandwidth *	0.21	0.20	0.19	nm
($\Delta\lambda_{3dB}$ | $\Delta\upsilon_{3dB}$)	26	25	23	GHz
Free Spectral Range *	11.72	7.74	7.74	nm
($\Delta\lambda_{FSR}$ | $\Delta\upsilon_{FSR}$)	1433	953	953	GHz

* at a central wavelength or frequency of 1560.6 nm or 192.1 THz, respectively.

From the best-simulated performance of AWG 1, the insertion loss was at a value of 17.4 dB with a level of crosstalk between adjacent channels of -25.5 dB and with a 3dB bandwidth of around 26% of the channel spacing (0.21 nm or 26 GHz), figure 3.7.

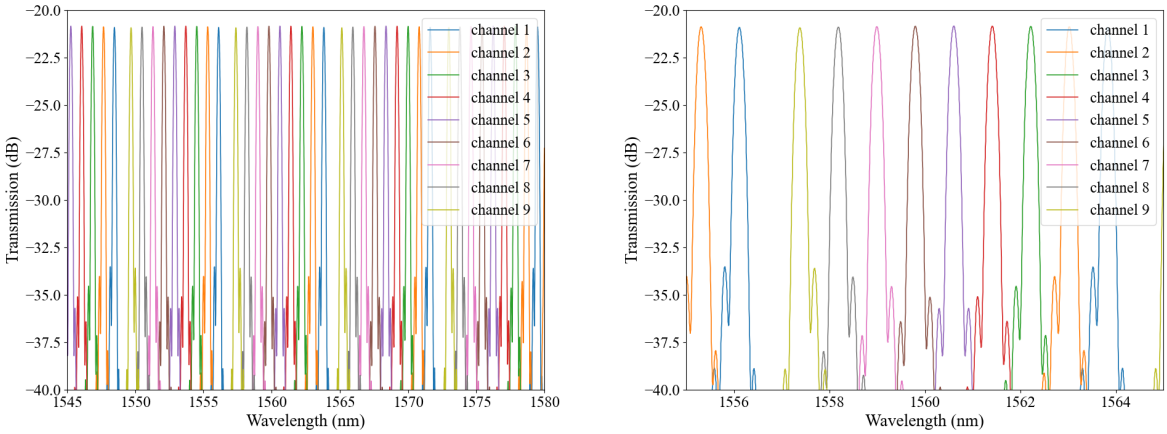

Figure 3.7: Simulated spectrum AWG011.

3.4 Measurements

From the FPR measurements, this structure was able to focus the input signal onto each arrayed waveguide, figure 3.8. It is possible to observe this effect when comparing the traveling signal, though a reference waveguide (WG ref) with the signal on each arrayed waveguide . The reference waveguide signal gives information about improper fibre-to-chip coupling. It was possible to verify a certain resonance in the waveguides close to the centre, this is due to a slight imperfection in the focal length. The birefringence of the X-cut LNOI will also impact the non-uniformity between arrayed waveguides and an adaptation of the model in terms of the birefringence nature of the X-cut LNOI has to be made.

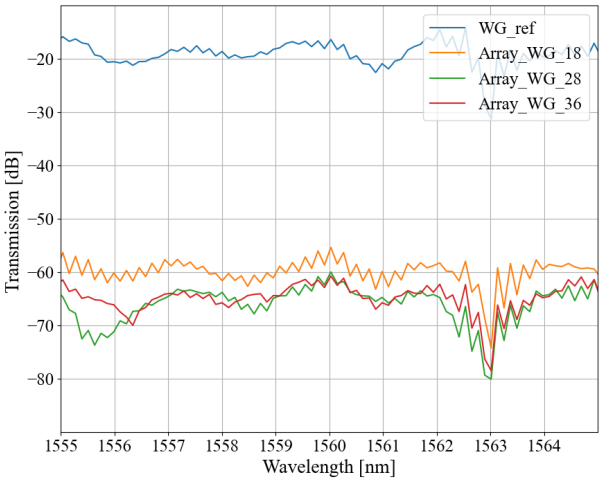

Figure 3.8: Measured spectrum FPR with 37 arrayed waveguides.

As previously explained the imbalanced Mach-Zehnder structure will result in a resonance pattern that has a periodicity (FSR), figure 3.9, that enables an indirect measurement of the ΔL equivalent to the experienced phase shift between the propagated light signals of adjacent arrayed waveguides. From this calculation, represented in table 3.3, it was possible to observe a mismatch between the architecturally designed ΔL and the one measured. This discrepancy is due to the birefringence of the X-cut LNOI, and so it is also important to adapt the modelling of the PHASAR region to account for this effect.

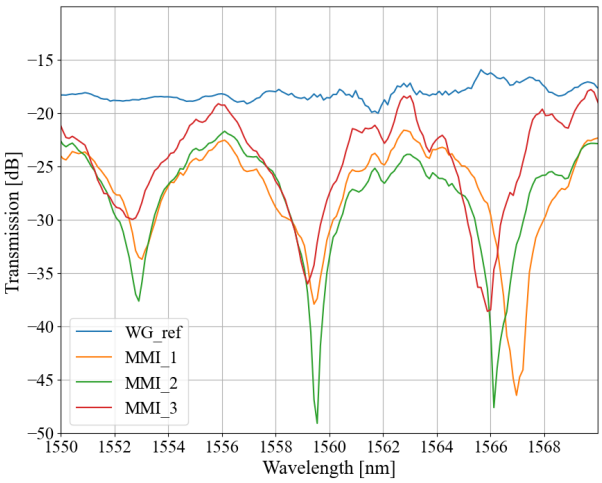

Figure 3.9: The measured spectrum of Imbalanced MZI.

Table 3.3: Imbalanced MZI measurements.

Parameter	MZI 1	MZI 2	MZI 3	Units
Free Spectral Range	7.54	6.57	6.69	nm
($\Delta\lambda_{FSR}$ | $\Delta\upsilon_{FSR}$)	928	809	824	GHz
ΔL Measured	142.6	163.4	160.6	μm
ΔL designed	158.3	158.4	158.4	μm

In regard to the AWG, its analysis was divided into functionality and performance. For the functionality, the bidirectional aspect, MUX, deMUX and routing were studied. The MUX could be verified by sweeping the input (applying signal at different input ports), while selecting a certain output (always measuring the same output port, figure 3.10 A. To verify the deMUX, the inverse approach can be taken, selecting a specific input and sweeping the output (measuring the response at each output port), figure 3.10 B. Even though this process is redundant given the AWG is a bidirectional reciprocal device, this double-checking was done.

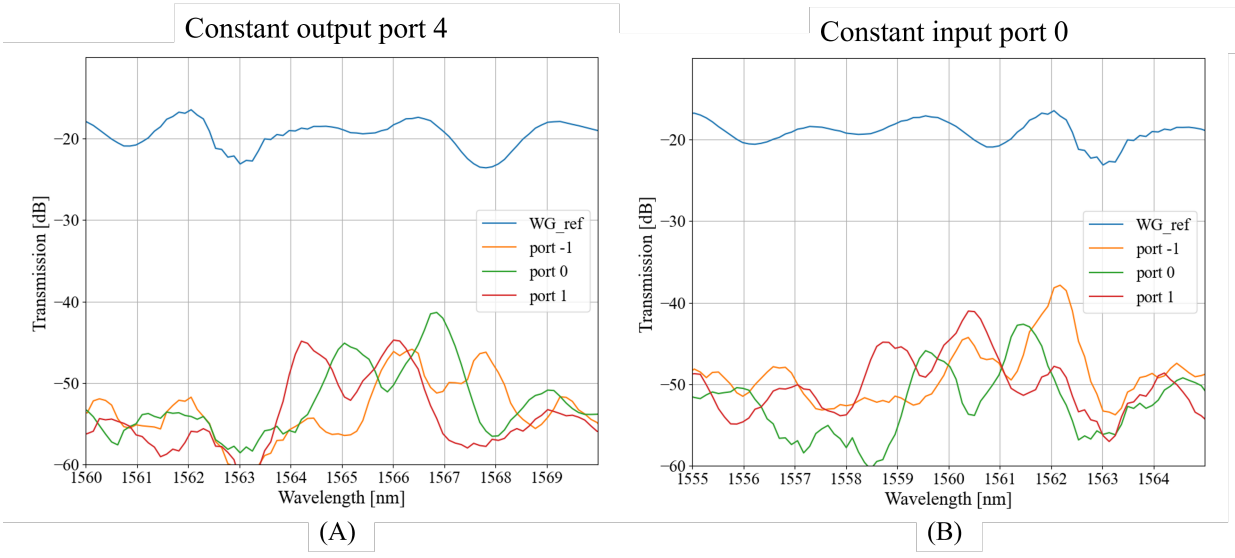

Figure 3.10: AWG 3 Functionality: (A) Multiplexing (MUX), (B) Demultiplexing (deMUX).

From these measurements, it is also possible to verify the routing, given that changing the input/output, from the central port to a port on the extremity (port 0 to port 4, respectively), resulted in a shift of wavelengths setting different wavelength channels at those central ports, figure 3.10.

While checking that the AWG functionality could be observed it was possible to verify the non-ideal performance of the device. When compared with the simulated behaviour that mismatch is confirmed, figure 3.11.

The most relevant performance shift is regarding the central wavelength, the channel

spacing and the shape of the channel. The central wavelength was 1557.0 nm in contrast to 1560.6 nm, the measured channel spacing was 0.9 nm and the simulated 0.8 nm. All these parameters are affected and controlled by the PHASAR region. Hence if the induced phase shift between each adjacent array waveguide is different than 2π the central wavelength and channel spacing will change. Given that the FPR is designed in accordance with the PHASAR region, then the interference in the secound FPR does not occur in the ideal manner, not aligned with the RC focal points. In this way, the peak shape is changed, broadening in relation to the simulation peak shape, given the measured bandwidth was 2.1 nm and the simulated 0.2 nm. This mismatch between the PHASAR theoretical and measured response was due to a shift in ΔL from the design model and the architectural gds model. In addition, the birefringence will also play a role, given the array waveguides are not optimized for that aspect.

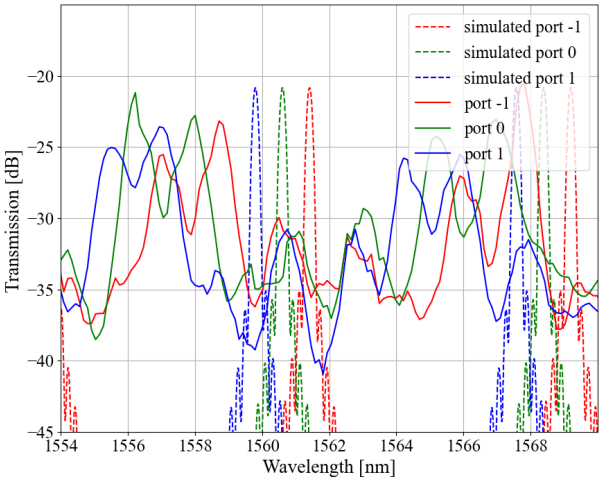

Figure 3.11: AWG 3 Measurement vs Simulation comparison.

Even though the performance and peak shape were not, ideal it was possible to extract the performance parameters, which are all explicitly indicated in table 3.4.

Table 3.4: AWG 3 Performance Parameters.

Performance parameter	Measured value	Simulated value	Units
Central channel	1557.0	1560.6	nm
(λ_0 | v_0)	192.5	192.1	THz
Channel Spacing *	0.9	0.8	nm
($\Delta\lambda_{ch}$ | Δv_{ch})	111.0	100.0	GHz
Free Spectral Range *	8.90	7.74	nm
($\Delta\lambda_{FSR}$ | Δv_{FSR})	1100	953	GHz
Insertion Loss (IL_0)	21.0	20.8	dB
Adjacent Crosstalk (Xtlk)	-9.6	-28.2	dB
3 dB Bandwidth *	2.10	0.19	nm
($\Delta\lambda_{3dB}$ | Δv_{3dB})	258	23	GHz

*at a central wavelength or frequency of 1560.6 nm or 192.1 THz, respectively.

4

Conclusion and Outlook

4.1 Conclusion

This thesis was the first step in designing an Arrayed Waveguide Grating building block. To develop such BB the physical and functional aspects of the AWG concept were studied and understood, as well as the current constraints that come from fabricating this device in the LNOI platform.

The AWG is a complex, multi-parameter device, which is quite intricate to design. The most typical design models were studied, in specific the Smit model, which was employed in this work.

The individual impact design of each AWG part, FPR and PHASAR was also studied, from a theoretical, simulation and practical approach. From this a set of gds design architectures were created that can be further studied in a deeper faction to clarify the physics of those structures, resulting in a more complete hypothesis over loss and crosstalk optimized architectures.

Regarding FPR varFDTD simulations were carried out allowing for verification of multiple FPR structures in terms of Rowland Circle design and focusing waveguide confinement and into the waveguides. In addition, these simulations also allow for a qualitative analysis of the losses, enabling the visualization of where these losses take place. Even though these simulations are versatile for different FPR structures, the used simulation program does not take into account both refractive indexes that describe the birefringence on the writing plane of the X-cut LNOI. Therefore, in future perspectives, a new simulation approach might be applied.

To simulate and retrieve an expected AWG spectrum, that can be compared with the measurement of a fabricated device, the AWG module of Lumerical Interconnect was used. From these simulations, in addition to simulating the spectrum expected to measure from a fabricated device, the effect of the most crucial design parameters on the performance of the device was also carried out. Which allowed the verification of the literature in regard to the importance of fabricating a device with a small waveguide spacing, both at the array and receiver/output waveguides, in order to attain a low-level Insertion loss. The effect

of the number of array waveguides was also understood regarding the Insertion loss and the shape of the channels.

In terms of measurements, an approach of studying each part in isolation and then the full AWG was considered. The FPR measurements ensured the proper focusing behaviour of that element, yet with some shift in response from the centre waveguide to a waveguide at the extremity of the array. This effect was due to the birefringence of the X-cut LNOI. To study the proper design of the PHASAR region an approach integrating MMI in an imbalanced MZI enabled the indirect measurement of length difference between two adjacent arrayed waveguides, that reflect the experienced phase shift between those two waveguides. From those measurements, it was possible to verify the impact of birefringence on the PHASAR in addition to the effect on FPR.

With the full AWG structure, the functionality of the device was tested and verified. Multiplexing, Demultiplexing, Routing and the bidirectionality of the device were observed. Confirming that the concept of AWG can be implemented on the LNOI platform. Regarding the performance, it was not measured the ideal response. The PHASAR was the component that mostly contributed to this situation, due to a mismatch between the model calculation of ΔL and the architecturally designed ΔL in the gds. The calculus of the bending radii of each arrayed waveguide was the location that was producing this result. Even though this aspect was corrected, it was not verified. Escalating this problem, the fact that this initial model does not take into account the X-cut LNOI birefringence will also generate a change in performance.

Though the performance of the fabricated AWG was not ideal, still it was an improvement on the only AWG on LNOI found in the literature, [59]. In terms of crosstalk, since the interference did not occur in a proper manner inside the second FPR, and the channel peaks were not well defined, the isolation of the channels was very poor. However, regarding the insertion loss, an improvement has been achieved comparing the AWG in the literature, [59], and the fabricated and described in this project, having insertion losses of 25 dB and 21 dB respectively. This performance value is also increased due to the improper interference pattern of the fabricated AWG.

4.2 Outlook and Future Perspectives

After the first stage of the creation and optimization of an Arrayed Waveguide Grating was formulated, a set of imminent procedures must be carried out to perfect this design model. The first step is the correction and verification of the mismatch, at the PHASAR, between the design model ΔL calculations and the architecture-designed gds.

In consequence, the model needs to be adapted to the LNOI X-cut birefringence. In the PHASAR this adaptation can be a calculation of an effective waveguide length in both y and z crystallographic directions. Having the 180-degree bending results in an arc length calculated using the average of both effective indexes or effective refractive indexes. However, the proper strategy might be more complex, for a simple approach as the one

expressed might create an overlapping of waveguides at the array. Optimizing the FPR for the birefringence is also a challenge given the circular shape of the Rowland curvature and the Array curvature will need to be adapted to represent two ellipses. Being the resulting FPR a sum of those two ellipses.

After finishing this step, the AWG BB should be complete and only more advanced optimizations can be carried out. Advanced optimization techniques include the tapering of the FPR waveguide interface, to reduce reflection inside the FPR, decreasing Insertion loss. Another approach also important to take into study, is the research of multiple architectures for the FPR RC, in order to reduce reflection at the sidewalls of the FPR decreasing unwanted interference patterns inside the FPR, improving insertion loss, crosstalk and overall AWG performance. After all these steps it will be possible to have an understanding of the constraints and limitations in the design, fabrication and performance of such a device in the LNOI platform. As previously stated, the non-steep sidewall angle of the waveguides created by the LNOI etching is not ideal and it is the primary limitation in achieving higher performances. For the LNOI to be competitive with other material platforms, this constraint needs to be met or overcome.

In order to have a more versatile device, the AWG BB can then be adapted to multiple applications and be stabilized in regard to environmental conditions.

Bibliography

[1] F. Ahlbom. "Analysis of the Performance of Different DWDM Filter Technologies for Mobile Fronthaul Applications". KTH ROYAL INSTITUTE OF TECHNOLOGY SCHOOL OF INFORMATION and COMMUNICATION TECHNOLOGY, 2016 (cit. on p. 8).

[2] Allwave.Lasers. *Athermal AWG DWDM*. URL: http://www.awlasers.com/Products/Integrated_photonics/AAWG/2016/1101/82.html (cit. on p. 3).

[3] R. Asquini et al. "Design of a wideband tunable AWG using electro-optic polymers and push-pull electrode configuration for ultrafast photonic switching applications". In: *Active and Passive Optical Components for WDM Communications III* 5246 (2003-08), p. 323. ISSN: 0277786X. DOI: 10.1117/12.511274 (cit. on p. 4).

[4] M. A. Baghban, S. K. Mahato, and K. Gallo. *Low-loss ridge waveguides in thin film lithium niobate-on-insulator (LNOI) fabricated by reactive ion etching*. KTH - Royal Institute of Technology, 2016 (cit. on p. 1).

[5] S. Benchabane et al. "Highly selective electroplated nickel mask for lithium niobate dry etching". In: *Journal of Applied Physics* 105 (9 2009). ISSN: 00218979. DOI: 10.1063/1.3125315 (cit. on p. 14).

[6] J. Bland-Hawthorn and A. Horton. "Instruments without optics: an integrated photonic spectrograph". In: vol. 6269. SPIE, 2006-06, 62690N. ISBN: 0819463345. DOI: 10.1117/12.670931 (cit. on p. 11).

[7] A. Boes et al. *Status and Potential of Lithium Niobate on Insulator (LNOI) for Photonic Integrated Circuits*. 2018-04. DOI: 10.1002/lpor.201700256 (cit. on pp. 2, 14, 15).

[8] C. A. Brackett. "Dense Wavelength Division Multiplexing Networks: Principles and Applications". In: *IEEE Journal on Selected Areas in Communications* 8 (6 1990), pp. 948–964. ISSN: 07338716. DOI: 10.1109/49.57798 (cit. on p. 8).

[9] J. Capmany et al. "Quantum model of light transmission in array waveguide gratings". In: *Optics Express* 21 (12 2013-06), p. 14841. ISSN: 1094-4087. DOI: 10.1364/oe.21.014841 (cit. on p. 9).

[10] C. Castellan et al. "Reflectance Reduction in a Whiskered SOI Star Coupler". In: *IEEE Photonics Technology Letters* 28 (17 2016-09), pp. 1870–1873. ISSN: 10411135. DOI: 10.1109/LPT.2016.2574364 (cit. on p. 4).

[11] C. Deng et al. "Broadband and compact polarization beam splitter in LNOI hetero-anisotropic metamaterials". In: *Optics Express* 29 (8 2021-04), p. 11627. ISSN: 1094-4087. DOI: 10.1364/oe.421262 (cit. on p. 13).

[12] C. Dragone. "Efficient N N Star Couplers using Fourier Optics". In: *Journal of Lightwave Technology* 7 (3 1989), pp. 479–489. ISSN: 15582213. DOI: 10.1109/50.16884 (cit. on p. 10).

[13] N. electronics. *NTT electronics 100GHz spacing athermal AWG*. URL: https://www.ntt-electronics.com/en/products/photonics/athermal-awg_100ghz.html (cit. on p. 3).

[14] M. R. Escalé. "Generation, Modulation and Detection of Light in Lithium Niobate Nanophotonic Devices". ETH, 2019 (cit. on pp. 12–14).

[15] M. R. Escalé et al. "Generation of 280 THz-spanningnear-ultraviolet light in lithiumniobate-on-insulator waveguideswith sub-100 pJ pulses". In: *APL Photonics* (2020). DOI: https://doi.org/10.1063/5.0028776 (cit. on p. 2).

[16] Fiberdyne.Labs. *DWDM AWG Athermal*. URL: https://www.fiberdyne.com/products/awg-dwdm-field-modules.html (cit. on p. 3).

[17] Z. Gong et al. "Optimal design of DC-based polarization beam splitter in lithium niobate on insulator". In: *Optics Communications* 396 (2017-08), pp. 23–27. ISSN: 00304018. DOI: 10.1016/j.optcom.2017.03.028 (cit. on p. 13).

[18] K. Grobe and M. Eiselt. *Wavelength Division Multiplexing: A Practical Engineering Guide*. Wiley, 2013. ISBN: 9781118755068 (cit. on p. 8).

[19] Q. Han, M. Menard, and W. Shi. "Superlattice Arrayed Waveguide Grating in Silicon Nitride". In: *IEEE Photonics Technology Letters* 32 (22 2020-11), pp. 1411–1414. ISSN: 19410174. DOI: 10.1109/LPT.2020.3028130 (cit. on p. 3).

[20] M. He et al. "High-performance hybrid silicon and lithium niobate Mach–Zehnder modulators for 100 Gbit s -1 and beyond". In: *Nature Photonics* 13 (5 2019-05), pp. 359–364. ISSN: 17494893. DOI: 10.1038/s41566-019-0378-6 (cit. on pp. 2, 14, 15).

[21] R. G. Hunsperger. *Integrated optics: Theory and technology: Sixth edition*. Springer US, 2009, pp. 1–513. ISBN: 9780387897745. DOI: 10.1007/b98730 (cit. on p. 7).

[22] C. K. Kao. "Optical fibre communication". In: *HKIE Transactions Hong Kong Institution of Engineers* 4 (2-3 1997), pp. 74–75. ISSN: 1023697X. DOI: 10.1080/1023697X.1997.10667728 (cit. on p. 4).

[23] M. Kawabe et al. "Microfabrication in LiNbO3 by ion-bombardment-enhanced etching." In: *J Vac Sci Technol* 15 (3 1978), pp. 1096–1098. ISSN: 0022-5355. DOI: 10.1116/1.569517 (cit. on p. 14).

[24] I. Krasnokutska, J.-L. J. Tambasco, and A. Peruzzo. "Nanostructuring of LNOI for efficient edge coupling". In: *Optics Express* 27 (12 2019-06), p. 16578. ISSN: 10944087. DOI: 10.1364/oe.27.016578 (cit. on pp. 1, 2).

[25] H. Li and R. Xie. "Effect of polarization sensitivity on ultrasmall silicon-on-insulator-based arrayed waveguide grating for fiber Bragg grating sensor interrogation". In: *Optical Engineering* 57 (06 2018-06), p. 1. ISSN: 15602303. DOI: 10.1117/1.oe.57.6.065103 (cit. on p. 2).

[26] H. Li et al. "Investigation of Ultrasmall 1 x N AWG for SOI-Based AWG Demodulation Integration Microsystem". In: *IEEE Photonics Journal* 7 (6 2015-12). ISSN: 19430655. DOI: 10.1109/JPHOT.2015.2501678 (cit. on p. 19).

[27] J. Li et al. "AWG optical filter with tunable central wavelength and bandwidth based on LNOI and electro-optic effect". In: *Optics Communications* 454 (2020-01). ISSN: 00304018. DOI: 10.1016/j.optcom.2019.124445 (cit. on pp. 4, 13).

[28] Y. Li et al. "Research of selective etching in LiNbO3 using proton-exchanged wet etching technique". In: *Materials Research Express* 7 (5 2020-05). ISSN: 20531591. DOI: 10.1088/2053-1591/ab8e70 (cit. on p. 1).

[29] J. T. Lin et al. "On-chip electro-optic tuning of a lithium niobate microresonator with integrated in-plane microelectrodes". In: *Science China: Physics, Mechanics and Astronomy* 58 (11 2015-11). ISSN: 16747348. DOI: 10.1007/s11433-015-5728-x (cit. on p. 14).

[30] J. Lin et al. "Advances in on-chip photonic devices based on lithium niobate on insulator". In: *Photonics Research* 8 (12 2020-12), p. 1910. ISSN: 2327-9125. DOI: 10.1364/prj.395305 (cit. on pp. 2, 14, 15).

[31] J. Lin et al. "Fabrication of high-Q lithium niobate microresonators using femtosecond laser micromachining". In: *Scientific Reports* 5 (2015-01). ISSN: 20452322. DOI: 10.1038/srep08072 (cit. on p. 14).

[32] J. M. Lourenço. *The NOVAthesis LaTeX Template User's Manual*. NOVA University Lisbon. 2021. URL: https://github.com/joaomlourenco/novathesis/raw/master/template.pdf (cit. on p. iii).

[33] H. C. Lu and W. S. Wang. "Cyclic arrayed waveguide grating devices with flat-top passband and uniform spectral response". In: *IEEE Photonics Technology Letters* 20 (1 2008-01), pp. 3–5. ISSN: 10411135. DOI: 10.1109/LPT.2007.910090 (cit. on p. 4).

[34] C.-S. Ma et al. *Analytical modeling of loss characteristics of a polymer arrayed waveguide grating multiplexer*. 2002, pp. 621–630. URL: www.elsevier.com/locate/optlastec (cit. on p. 10).

[35] M. Mahmoud et al. "Lithium Niobate Electro-Optic Racetrack Modulator Etched in Y-Cut LNOI Platform". In: *IEEE Photonics Journal* 10 (1 2018-02). ISSN: 19430655. DOI: 10.1109/JPHOT.2018.2797244 (cit. on pp. 2, 15).

[36] P. Muñoz, D. Pastor, and J. Capmany. "Modeling and design of arrayed waveguide gratings". In: *Journal of Lightwave Technology* 20 (4 2002-04), pp. 661–674. ISSN: 07338724. DOI: 10.1109/50.996587 (cit. on p. 9).

[37] J. Park et al. "New design for low-loss star couplers and arrayed waveguide grating devices". In: *IEEE Photonics Technology Letters* 14 (5 2002-05), pp. 651–653. ISSN: 10411135. DOI: 10.1109/68.998714 (cit. on pp. 4, 12).

[38] G. Poberaj et al. "Lithium niobate on insulator (LNOI) for micro-photonic devices". In: *Laser and Photonics Reviews* 6 (4 2012-07), pp. 488–503. ISSN: 18638880. DOI: 10.1002/lpor.201100035 (cit. on p. 14).

[39] D. Pohl et al. "100-GBd Waveguide Bragg Grating Modulator in Thin-Film Lithium Niobate". In: *IEEE Photonics Technology Letters* 33 (2 2021-01), pp. 85–88. ISSN: 19410174. DOI: 10.1109/LPT.2020.3044648 (cit. on pp. 2, 15).

[40] D. Pohl et al. "An integrated broadband spectrometer on thin-film lithium niobate". In: *Nature Photonics* 14 (1 2020-01), pp. 24–29. ISSN: 17494893. DOI: 10.1038/s41566-019-0529-9 (cit. on p. 2).

[41] P. Rabiei and P. Gunter. "Optical and electro-optical properties of submicrometer lithium niobate slab waveguides prepared by crystal ion slicing and wafer bonding". In: *Applied Physics Letters* 85 (20 2004-11), pp. 4603–4605. ISSN: 00036951. DOI: 10.1063/1.1819527 (cit. on p. 13).

[42] J. M. Senior. *Optical Fiber Communications Principles and Practice Third Edition*. 3rd ed. Pearson Education Limited, 2009. URL: www.pearson-books.com (cit. on pp. 15, 16).

[43] D. Seyringer et al. *Comparison of Silicon Nitride based 8-channel 100-GHz AWGs applying different AWG Structures*. 2019. URL: https://www.researchgate.net/publication/334131204 (cit. on p. 2).

[44] B. Shahi et al. "Recent advances in oprical network technologies and its role in telecommunication industry". In: *International Journal of Research -GRANTHAALAYAH* 5 (4RACEEE 2017-04), pp. 15–22. ISSN: 2394-3629. DOI: 10.29121/granthaalayah.v5.i4raceee.2017.3317 (cit. on p. 5).

[45] K. Shang et al. "Low-Loss Compact Silicon Nitride Arrayed Waveguide Gratings for Photonic Integrated Circuits". In: *IEEE Photonics Journal* 9 (5 2017-10). ISSN: 19430655. DOI: 10.1109/JPHOT.2017.2751003 (cit. on p. 3).

[46] C. Shen et al. "A comparative study of dry-etching nanophotonic devices on a LiNbO3-on-insulator material platform". In: (2021-02), p. 13. ISSN: 1996756X. DOI: 10.1117/12.2590415 (cit. on pp. 1, 2).

[47] M. K. Smit and C. V. Dam. *PHASAR-Based WDM-Devices: Principles, Design and Applications*. 1996 (cit. on pp. 2, 9, 12, 17).

[48] M. K. Smit. "Progress in AWG design and technology". In: *Proceedings of WFOPC2005 - 4th IEEE/LEOS Workshop on Fibres and Optical Passive Components* 2005 (2005), pp. 26–30. DOI: 10.1109/WFOPC.2005.1462095 (cit. on p. 12).

[49] A. Sugita et al. "Very low insertion loss arrayed-waveguide grating with vertically tapered waveguides". In: *IEEE Photonics Technology Letters* 12 (9 2000-09), pp. 1180–1182. ISSN: 10411135. DOI: 10.1109/68.874228 (cit. on p. 4).

[50] F. Sulser et al. *Photonic crystal structures in ion-sliced lithium niobate thin films References and links*. 2009 (cit. on p. 13).

[51] A. V. Syuy et al. "Optical properties of lithium niobate crystals". In: *Optik* 156 (2018-03), pp. 239–246. ISSN: 00304026. DOI: 10.1016/j.ijleo.2017.10.136 (cit. on p. 12).

[52] M. Tamura and S. Yoshikado. "Etching characteristics of LiNbO 3 crystal by fluorine gas plasma reactive ion etching". In: *Science and Technology of Advanced Materials* (2001). URL: www.elsevier.com/locate/stam (cit. on p. 14).

[53] L. Vivien and L. Pavesi. *Handbook of silicon photonics*. CRC Press, 2013 (cit. on p. 10).

[54] S. Weng et al. "SOI-based arrayed waveguide grating with extended dynamic range for fiber Bragg grating interrogator". In: *Optical Fiber Technology* 68 (2022-01). ISSN: 10685200. DOI: 10.1016/j.yofte.2021.102815 (cit. on pp. 2, 3).

[55] R. Wu et al. "Long low-loss-litium niobate on insulator waveguides with sub-nanometer surface roughness". In: *Nanomaterials* 8 (11 2018-11). ISSN: 20794991. DOI: 10.3390/nano8110910 (cit. on p. 2).

[56] H. Xu et al. "Proposal for an ultra-broadband polarization beam splitter using an anisotropy-engineered Mach-Zehnder interferometer on the x-cut lithium-niobate-on-insulator". In: *Optics Express* 28 (8 2020-04), p. 10899. ISSN: 1094-4087. DOI: 10.1364/oe.390075 (cit. on p. 15).

[57] M. Xu et al. "High-performance coherent optical modulators based on thin-film lithium niobate platform". In: *Nature Communications* 11 (1 2020-12). ISSN: 20411723. DOI: 10.1038/s41467-020-17806-0 (cit. on pp. 2, 13).

[58] Y. Yang et al. "Thermo-Optically Tunable Silicon AWG with above 600 GHz Channel Tunability". In: *IEEE Photonics Technology Letters* 27 (22 2015-11), pp. 2351–2354. ISSN: 10411135. DOI: 10.1109/LPT.2015.2464073 (cit. on p. 4).

[59] S. J. B. Yoo, P. Mathias, and L. Guangyao. "A Compact Thin-Film Lithium Niobate Platform with Arrayed Waveguide Gratings and MMIs". In: *IEEE Optical Society of America* (2018) (cit. on pp. 4, 5, 30).

[60] J. X. Zhou et al. "Electro-Optically Switchable Optical True Delay Lines of Meter-Scale Lengths Fabricated on Lithium Niobate on Insulator Using Photolithography Assisted Chemo-Mechanical Etching". In: *Chinese Physics Letters* 37 (8 2020-07). ISSN: 17413540. DOI: 10.1088/0256-307X/37/8/084201 (cit. on p. 14).

[61] D. Zhu et al. "Integrated photonics on thin-film lithium niobate". In: *Advances in Optics and Photonics* 13 (2 2021-06). ISSN: 1943-8206. DOI: 10.1364/AOP.411024 (cit. on p. 15).

[62] J. Zou et al. "Silicon-Based Arrayed waveguide gratings for WDM and spectroscopic analysis applications". In: *Optics and Laser Technology* 147 (2022-03). ISSN: 00303992. DOI: 10.1016/j.optlastec.2021.107656 (cit. on p. 10).